Uniform propagation of cathode-directed surface ionization waves at atmospheric pressure

T Darny, D. Babonneau, S Camelio, D Pai

Uniform propagation of cathode-directed surface ionization waves at atmospheric pressure

T. Darny[1], D. Babonneau[2], S. Camelio[2] and D. Z. Pai[1]

[1]*Institut Pprime, Département Fluide, Thermique et Combustion, CNRS UPR 3346, Université de Poitiers, ISAE-ENSMA, SP2MI, TSA 51124, 86073 Poitiers Cedex 9, France*

[2]*Institut Pprime, Département Physique et Mécanique des Matériaux, CNRS UPR 3346, Université de Poitiers, ISAE-ENSMA, SP2MI, TSA 41123, 86073 Poitiers Cedex 9, France*

Abstract

The uniform propagation of positive-polarity surface plasmas in air at atmospheric pressure has been achieved using a multi-layer structure, consisting of a silicon wafer covered by a 1 µm thick dielectric SiO_2 layer as a propagation surface. Instead of the branched streamers observed in the same conditions when using conventional bulk dielectric surfaces, the plasma exhibits a homogenous ring-shaped structure with a high degree of reproducibility and stability. The plasma is generated by applying nanosecond positive voltage pulses to a tungsten wire touching the dielectric surface. The plasma has been imaged in single shot operation at high spatial resolution with an ultraviolet reflective microscope coupled with a fast intensified charge-coupled device camera. Time-and space-resolved optical emission spectroscopy shows that the homogenous ring corresponds to the propagation of an ionization front with a region of high N_2^+* emission. We discuss the origin of the ring-shaped ionization wave, considering the role of the Si-SiO_2 interface and the effect of illumination by an external light source. The ring ionization wave may result from branching inhibition, due to a photoelectric effect at the interface created by the photons emitted by the plasma. The generation of stable uniform surface ionization waves, in ambient air at atmospheric pressure, could be of interest for further advanced plasma-surface interaction studies or flow control applications.

1. Introduction

Surface dielectric barrier discharges (SDBD) have been of growing interest in the past 20 years, especially with the development of numerous applications in flow control [1]–[3], plasma assisted combustion [4], surface treatment for activation [5], materials processing [6] and many other examples in both fundamental and applied research [7]. In order to optimize the efficiency of plasma actuation, several authors have studied the influence of the propagation surface itself on the plasma dynamics. As shown by Roth and Dai [8] and Fine *et al* [9], the use of a higher permittivity material could enhance the momentum transfer of the actuator. Opaits *et al* [10] modified the plasma propagation surface with a slightly conductive silicon coating to evacuate surface charge. Starikovskiy *et al* [11], [12] developed a semiconducting surface dielectric barrier discharge, with the propagation surface designed as a diode array. The authors showed that reverse breakdown could be suppressed with this configuration. With a wide range of conductive layers (distilled water, saline solutions, alcohols)

covering Kapton dielectric films, Leonov *et al* [13] discovered that the surface conductivity affects the plasma differently depending on the RC time constant (where R is the plasma resistance and C is the actuator capacitance) of the liquid surface relative to the characteristic time of the nanosecond voltage waveform. When the liquid surface reacted fast enough, *i.e.* with a small RC time constant, the authors showed that it acted like an extension of the high voltage electrode, which led to increased energy storage in the surface. The authors emphasized the relationship between the plasma and the propagation surface itself for the further development of plasma actuators for flow control.

In atmospheric-pressure air, the plasma generated with SDBDs typically exhibits a non-uniform structure. With a nanosecond pulsed surface discharge in synthetic air, Stepanyan *et al* [14] have shown that the synchronized propagation of multiple streamers from the cathode at atmospheric pressure could lead to a quasi-uniform plasma. At higher pressure and voltage amplitude, the structure transforms from quasi-uniform to filamentary. Recently, Ding *et al* [15] have shown that this transition was a function of the applied high voltage and amplitude and can be considered as a general feature for any mixture containing molecular gases. The authors also reported that the transition from quasi-uniform to filamentary occurs with characteristic changes to the optical emission spectra, with the disappearance of molecular excitation bands and the emergence of dominant atomic lines emission. The transition is also marked by an increase in the current up to several amperes per filament. SDBD at even higher pressure (>1 MPa) can enter a field-emitting Townsend regime in which optical emission spectra are purely continuum in nature [16]–[18]. With the recent development of optical laser diagnostics, the electric field components associated with the surface ionization wave propagation are not only to the subject of numerical studies [19], [20] but have also been successfully measured [21], [22].

Nevertheless, despite considerable progress, the understanding of plasma propagation dynamics and interactions with the surface is still a challenge. One reason is that streamer branching often impedes the reproducibility of a single discharge event. Petrishchev *et al* [23] generated reproducible and homogenous ionization waves but only at low pressure (between 5 Torr and 100 Torr). In a point to plane discharge configuration, Takahashi *et al* [24] succeeded in controlling the branching of positive streamers by using external laser irradiation. When the plasma propagated in the illuminated region, the higher ionization in this region suppressed the branching of the streamer. Nijdam *et al* [25] also demonstrated that a positive streamer could be guided by preionization from the free electrons generated by laser illumination. The studies [24], [25] concern volume discharges. To our knowledge, there is no such study on SDBD.

Recently, Pai *et al* [26] have shown that it was also possible to use as a propagation surface a thin film (40 nm) of alumina deposited on a silicon wafer. Conversely to what it is observed on the silicon without the film, the plasma is not confined to the anode anymore and can propagate on the surface. In this paper, we continue the development of these multi-layer propagation surfaces and we report to the best of our knowledge the first observation of a homogenous surface ionization wave using positive ns pulses in ambient air at atmospheric pressure, in a SDBD configuration. The plasma propagates without any branches and exhibits very good reproducibility from pulse to pulse. This is achieved by using a particular multi-layer as a propagation surface. Instead of a classical bulk dielectric, a silicon wafer covered by a 1 µm thick dielectric layer of SiO_2 is used. The experimental setup is presented in section 2. The results and discussion are detailed in section 3, where we compare the plasma generated on glass versus the Si-SiO_2 bilayer using time- and space-resolved emission spectroscopy. We propose a mechanism for the ring ionization wave, emphasizing the influence of the interface between the silicon and the SiO_2 layer. To support this explanation, we also perform

experiments on other multi-layer structures and examine the effect of an external illumination source on plasma propagation. Concluding remarks are presented in section 4.

2. Experimental setup

Due to small dimensions of the plasma propagation, highly time- and space-resolved diagnostics are essential to resolve the propagation dynamics, such as cross correlation spectroscopy with sub-ns and sub-mm resolution [27], [28] or microscopic imaging to magnify the image [29]. In this paper, we use a reflective ultraviolet (UV) microscope objective based on a Schwarzschild or inverse Cassegrain design [30]. Briefly, it is based on a concentric two-mirror system whose magnified image is free from chromatic aberration and corrected for spherical aberration, coma, and astigmatism. Figure 1 (a.) shows the discharge geometry in an asymmetric SDBD arrangement facing the microscope objective used for imaging (b.) and optical emission spectroscopy (OES) (c.). For OES the slit was 100 µm wide.

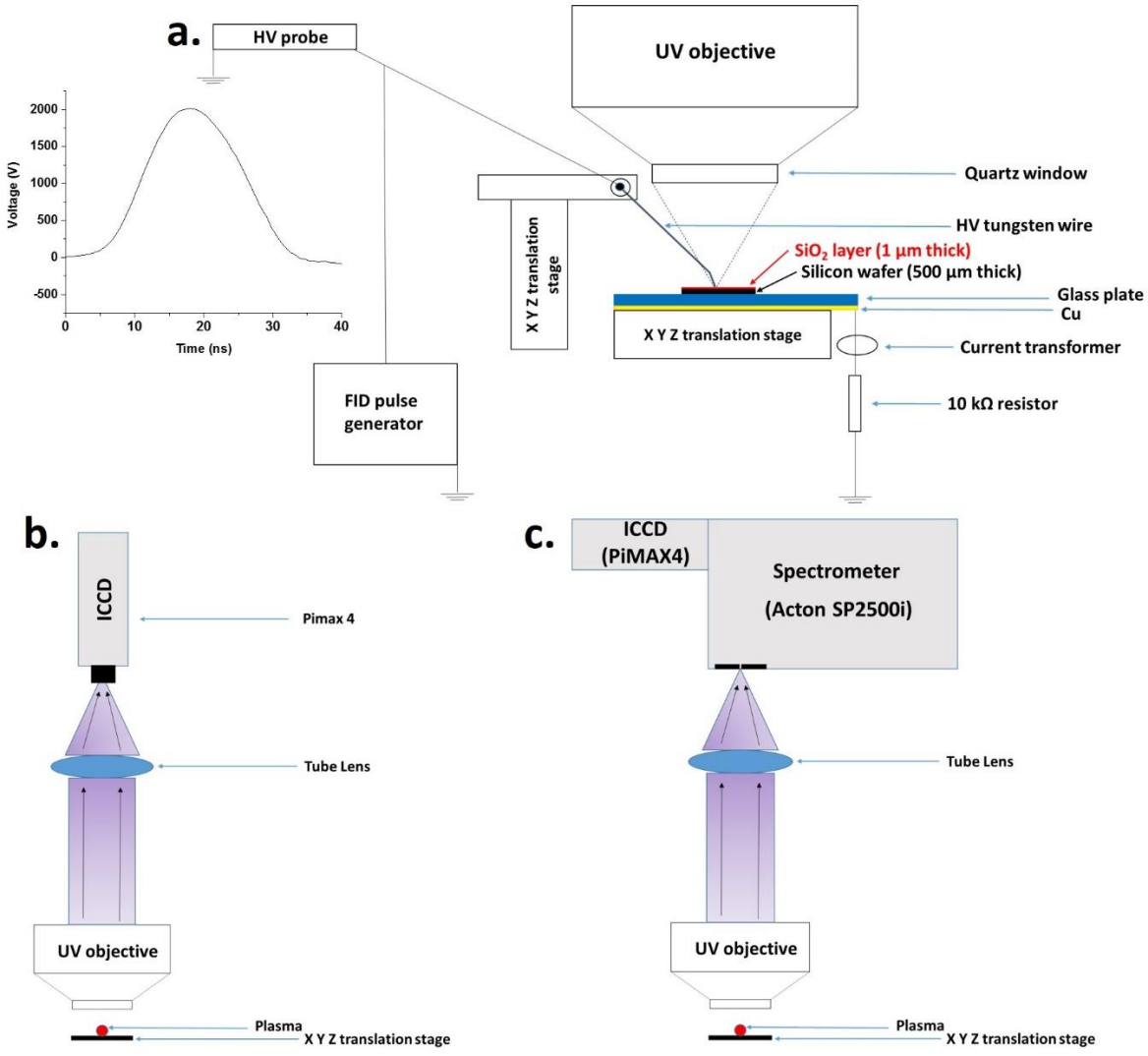

Figure 1 : Schematic view of the SDBD geometry and the reflective microscope, with the ns voltage pulse waveform used (a). Schematic view of the microscopy optical bench used for fast ICCD imaging (b.). Time- and space-resolved optical emission spectroscopy is performed when the ICCD camera is mounted on the spectrometer (c).

The plasma is generated in ambient air at atmospheric pressure. The anode is connected to a high voltage (HV) pulse generator (FID Technology FPG 40-30 NK) that produces positive pulses of 30-ns duration with a pulse repetition rate set at 50 Hz in all cases. The applied voltage was measured using a passive probe (Lecroy PPE 6 kV) with 400 MHz bandwidth. All current and voltage signals were acquired using an oscilloscope with 2-GHz bandwidth (Lecroy Waverunner 204 MXI). The anode is a tungsten wire (Goodfellow 99.95% purity) with a diameter of about 100 µm, placed into mechanical contact with the surface using a micrometric translation stage. The propagation surface is a silicon wafer (500 µm thickness, p-type) covered by a 1-µm thick layer of thermally grown SiO_2 (Wafernet). For the sake of clarity, the Si-SiO_2 assembly will be referred to as the "Si-SiO_2 bilayer". To limit the current and surface damage, the bilayer is fixed onto a borosilicate glass plate (1 mm thick) that is grounded by copper adhesive. For comparisons with plasma propagation on the glass plate, the bilayer is removed for direct contact between the glass plate and the wire. A 10 kΩ series resistor is also used to reduce the current further. The plasma can then be switched on for several hours without damaging the surface at a repetition rate of 50 Hz and voltage amplitude up to 4 kV (compared to only a few minutes without the glass plate). A current transformer (Bergoz CT-D5.0, 400 Mhz bandwidth) was used to follow in real time the damage to the surface during imaging and OES measurements. When the surface is damaged, the current waveform becomes highly unstable from pulse to pulse. All devices are synchronized using a generator delay (Stanford Research Systems model DG645).

The objective (Beck Optronic Solutions, model 5002) possesses a focal length of 13.4 mm, numerical aperture of 0.50 and working distance of 23.2 mm. The aluminum mirrors reflect efficiently from 200 nm to 10 µm. The surface is set at the focal point of the microscope objective, with a second micrometric translation stage (Figure 1(a.)). The tube lens is a plano-convex achromatic doublet with a 125 mm effective focal length and a 345 nm- 700 nm antireflection coating. It is used to form the image onto the intensified charge-coupled device (ICCD) detector (Princeton PIMAX4) or entrance slit of the spectrometer (Acton SP2500i), respectively for imaging (Figure 1(b.)) or optical emission spectroscopy (OES) (Figure 1(c.)). In our experimental conditions, the magnification is 9.3X. The error on the size on ICCD images is estimated to be 3 µm.

3. Results and discussion

3.1 Plasma propagation dynamics of the Si-SiO_2 bilayer versus glass SDBD

Figure 2 shows the plasma propagation on the Si-SiO_2 bilayer as a function of time, with the applied voltage set at 2 kV. The dark region at the center of each frame is the contact point of the anode tip. The outer diameter of the discharge is defined as the average of the values from the top to the bottom and from the left to right of the luminous regions. The propagation speed is the distance traveled by the plasma between two images, divided by their relative time delay, averaged over four locations (top, bottom, right, and left).

Several distinct phases are visible during plasma propagation:

- Just after plasma ignition at 10 ns, the plasma propagates in a fully homogeneous way until 14 ns. At 14 ns, the diameter is 390 µm. This phase will be referred to as the homogenous propagation phase.
- The region close to the wire starts to dim slightly at 15 ns, which is clear at 16 ns. It results in the formation of a ring structure. The ring continues to propagate up to 24 ns. From 15 ns to 24 ns, the outer diameter increases from 425 µm to 552 µm. This phase will be referred to as the ring propagation phase.

- From 29 ns to 59 ns, a secondary plasma is ignited and propagates. This secondary plasma is homogenous and does not exhibit a clear ring structure. At 59 ns, the diameter is 506 µm.

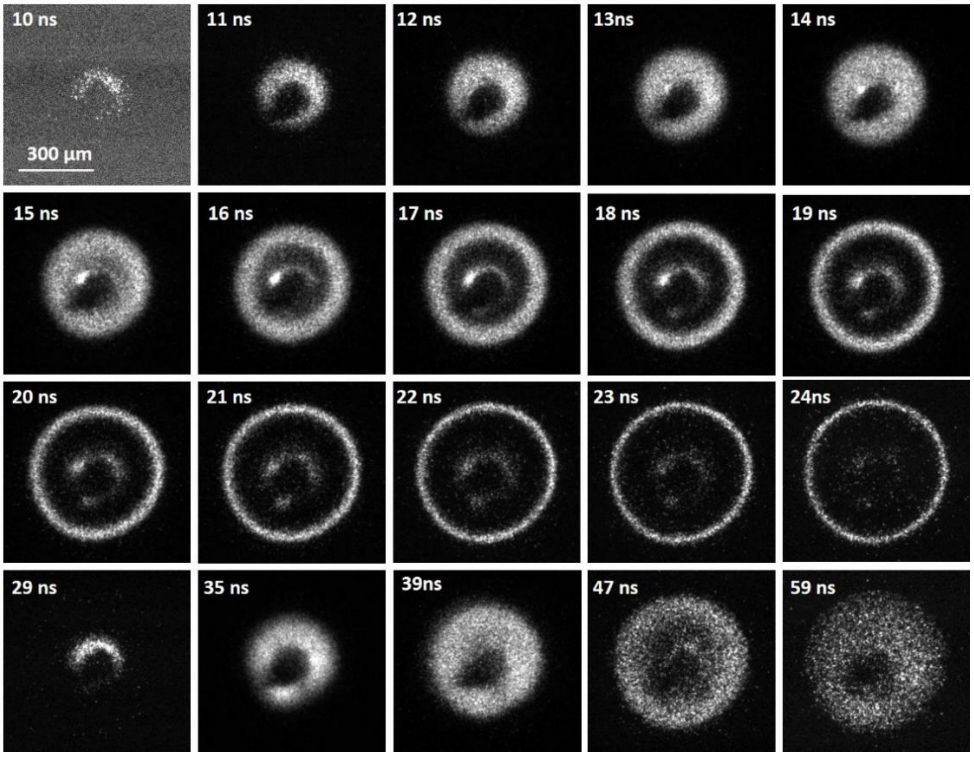

Figure 2 : Single-shot ICCD images of the plasma generated on the Si-SiO_2 bilayer, as a function of the delay relative to the start of the voltage pulse at 0 ns. The applied voltage is 2 kV. The exposure time for each image is 4 ns.

The plasma propagation velocity is 2.5 10^6 cm/s (±10 %) during the homogenous phase from 10 ns to 14 ns and drops during the ring propagation to 9.6 10^5 cm/s (±6 %) from 15 ns to 19 ns and then down to 4.5 10^5 cm/s (±9 %) from 20 ns to 24 ns. By 24 ns, the ring appears to stop expanding. From 29 ns to 47 ns, the propagation velocity of the secondary plasma is 8.3 10^5 cm/s (±4 %). The ring thickness progressively decreases during propagation (90 µm at 16 ns, 67 µm at 19 ns and finally 37 µm at 24 ns).

A corona discharge is also visible close to the anode tip, presumably because the corona onset threshold is reached at the triple junction between the anode tip, the Si-SiO_2 surface, and the air. The number and stability of the coronas depend on both the tip shape and the condition of the mechanical contact between the tip and the surface.

Figure 3 shows the effect of the applied voltage on the ring propagation distance. The plasma is imaged at the end of the ring propagation phase, at the same time delay Δt after plasma ignition, for each applied voltage value. Compared to the ignition time with the applied voltage set at 2 kV, the plasma is respectively ignited 3 ns later and 1 ns sooner at 1 kV and 3 kV.

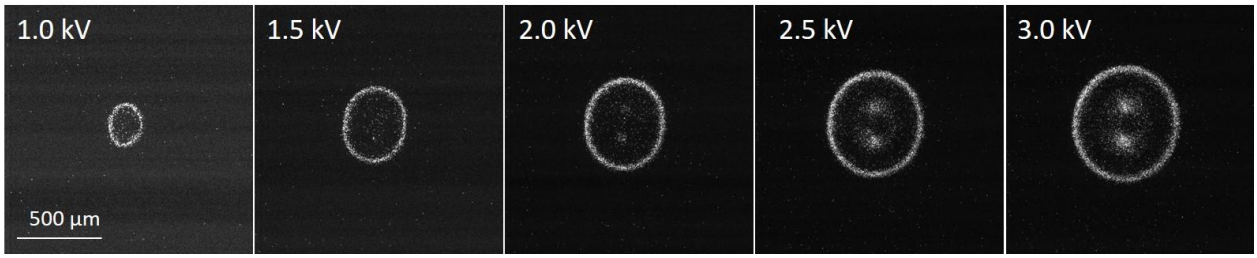

Figure 3 : Single shot ICCD images of the plasma for applied voltages from 1.0 kV to 3.0 kV. All images are taken close to the end of the ring propagation phase (Δt=12 ns). The exposure time for each image is 4 ns.

The propagation distance is directly related to the voltage amplitude. From 1.5 kV to 3 kV, the ring diameter from top to bottom increases from 456 µm to 698 µm. Between 1.0 and 1.5 kV, the increase is sharper, from 262 µm to 456 µm. Compared to Figure 2 at 2 kV, the ring shape is more elliptical. It could be due to the presence of two coronas at the anode, rather than one. However, the ring becomes more circular at greater distance from the anode. The ring thickness also increases with the voltage amplitude from 28 µm at 1.0 kV to 42 µm at 3.0 kV, which is 33 % higher.

Figure 4 (a.) compares ICCD images of the plasma for the glass plate and for the Si-SiO_2 bilayer when the applied voltage is 2 kV, which is close to the breakdown threshold for the glass plate (1.8 kV in our conditions). For the Si-SiO_2 bilayer the threshold is only about 650V. The plasma is consequently ignited about 6 ns later on the glass plate. In order to compare the pulse–to-pulse reproducibility, three images with the same time delay are selected in Figure 4 (a.), when the plasma propagation is well underway for both types of surfaces.

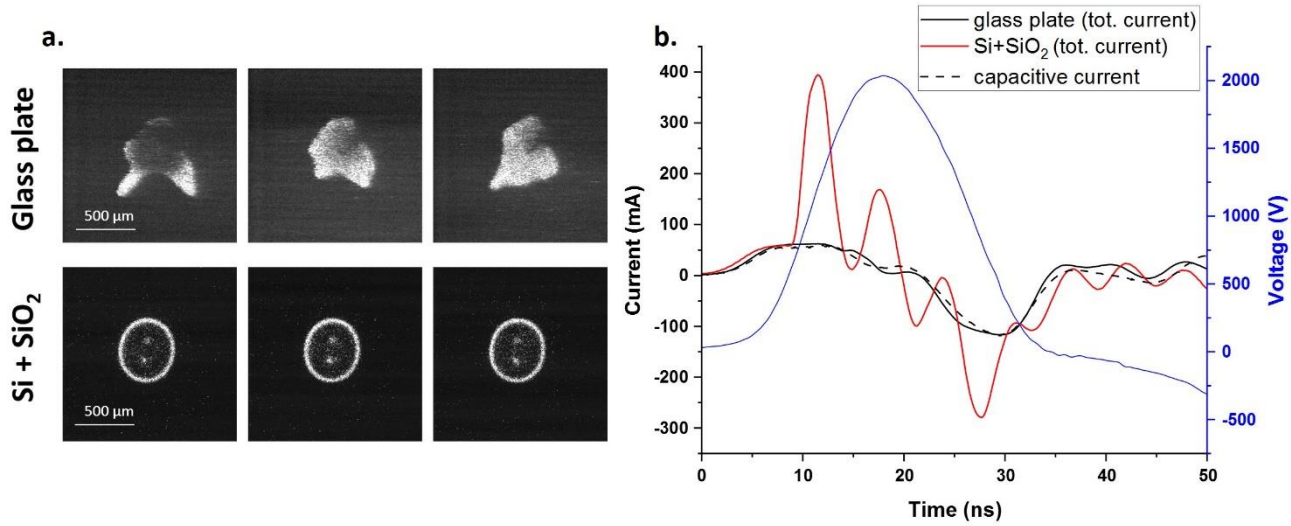

Figure 4 : Single shot ICCD images of the plasma at a fixed time delay (21 ns) with the applied voltage being 2 kV (a.). Applied voltage waveform (blue solid) with the current waveforms of the Si-SiO_2 bilayer (red solid) and glass plate (black solid) cases, as well as the capacitive current (dashed) (b.). The exposure time for each image is 4 ns.

On the glass plate, the plasma propagates in a branched way. The distribution of these branches over the surface changes from one pulse to another. This is a classic case of streamer propagation, particularly when cathode directed. Because the applied voltage here is only 0.2 kV higher than the breakdown voltage, the plasma remains close to the wire with a low level of branching. Furthermore, even for a fixed time delay, the branches were also imaged either in the early or late phase of their propagation, which is due to the jitter of breakdown. Conversely, for the Si-SiO_2 bilayer in the same

operating conditions, the plasma exhibits the stable ring shape with high pulse-to-pulse reproducibility.

Figure 4 (b.) shows the total current for the Si-SiO_2 bilayer and the glass plate cases, which includes the capacitive and discharge currents, as well as oscillations possibly due to additional parasitic elements introduced by the plasma. With the glass plate, the plasma contribution to the total current is weak compared to the capacitive current. The two curves start to diverge at 15 ns, when the plasma ignites on the glass plate. However, the plasma-induced contribution is higher for the Si-SiO_2 bilayer. The plasma is ignited during the rising edge of the voltage pulse and is associated with a sharp current increase from 67 mA at 9 ns to 394 mA at 11.5 ns. The secondary plasma depicted in Figure 2 is ignited at the falling edge of the voltage pulse and is associated with a negative current peak of -279 mA. The value of the current depicted in Figure 4 (b.) is one order of magnitude lower than the current of filaments reported by Ding *et al* [15], but higher than those usually reported for streamers in SDBD [31]. In [31], Hoder *et al* have clarified the charge transfer mechanism for SDBDs, with a detailed experimental analysis. Here, we must point out that due to the particular Si-SiO_2 bilayer features (see Figure 8), the large current peaks in Figure 4 (b.) may result from discharge current together with current originating from within the Si-SiO_2 bilayer.

Figure 5 compares ICCD images of the plasma generated on the glass plate and on the Si-SiO_2 bilayer for higher applied voltage (3 kV). As explained in Figure 4, the plasma ignition time is not the same between the two cases. In order to simplify the description, the time delay Δt indicated here is relative to the moment of plasma ignition for each type of surface.

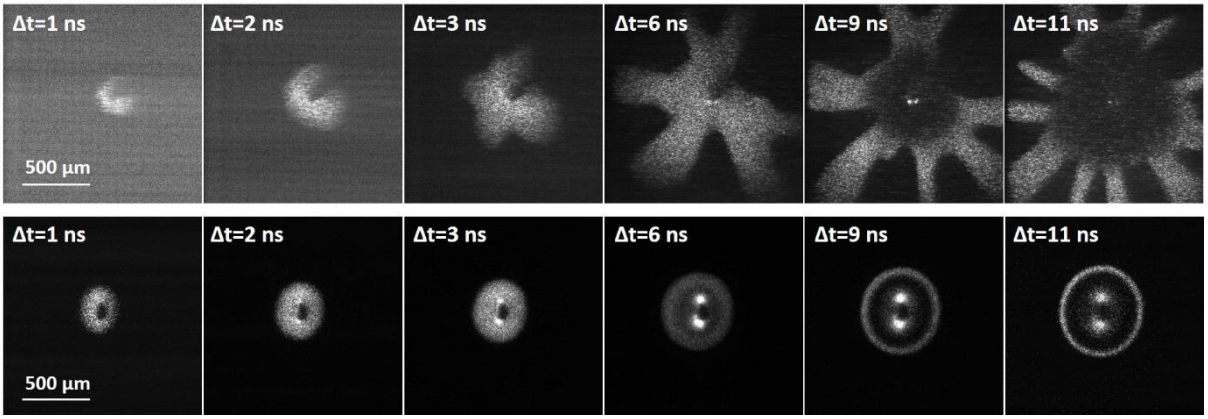

Figure 5 : Single shot ICCD images of the plasma generated on the glass plate (top row) and on the Si-SiO_2 bilayer (bottom row). The time delay Δt is relative to the moment of plasma ignition. The applied voltage is 3 kV. The exposure time for each image is 4 ns.

On the glass plate, the plasma is homogenous for the first 2 ns after plasma ignition. Then it starts to branch at Δt=3 ns, quickly leaving the field of view (Δt=6 ns). Between Δt=6 ns ns and Δt=7 ns (not shown) the region close to the wire starts to go dark while the streamer heads continue to propagate out of the field of view. Compared to Figure 4, the propagation distance is greater and the velocity is higher (in the range of 10^7 cm/s), because the voltage amplitude is higher. For the same reason, the level of branching is also higher.

Conversely, on the Si-SiO_2 bilayer, the branches do not appear at Δt=3 ns and the plasma stays homogenous. Then the ring appears and propagates, as depicted previously in Figure 2. Comparing the two cases shown in Figure 5, the propagation distance is also clearly lower on the Si-SiO_2 bilayer. Because the ignition time is not the same for the plasma on the two surfaces, the voltage amplitudes during the plasma propagation are also not the same. Between Δt=3 ns and Δt=6 ns after the plasma ignitions, the voltage is close to its maximum amplitude for the glass plate, while it is in the rising edge

on the Si-SiO_2 bilayer (as depicted in Figure 4 (b.)). Consequently, it is not possible to attribute the slower propagation velocity observed on the Si-SiO_2 bilayer only to a surface effect.

Also, the light emission is more intense on the Si-SiO_2 bilayer, which is consistent with the current amplitude depicted in Figure 4 (b.). The width of the streamers at Δt=11 ns ranges from ~90 µm to a few hundred µm, which is higher than the ring thickness at Δt=11 ns (40 µm).

Compared to plasma propagation on bulk dielectrics, the major difference is the complete absence of branching and a high pulse to pulse reproducibility. The propagation distance is also reduced. On the glass plate, we observed that the IW starts homogenously and then branches 2 ns after the plasma ignition (Figure 5). This phenomenon has been previously simulated by Xiong and Kushner [32]. On the Si-SiO_2 bilayer however, it seems that the branching is fully inhibited and the plasma keeps its initial homogenous state.

3.2 Plasma spectral emission for the case of the Si-SiO_2 bilayer

Figure 6(a.) shows the image of the discharge at 19 ns, for the conditions of Figure 2. The image was taken using the OES setup of Figure 1(c) with the slit completely open and the grating positioned to reflect light in zero order. Also indicated is the portion of the image spatially filtered by the slit when adjusted to the width used for OES. The filtered image was diffracted by the spectrometer to produce the spatially resolved emission spectrum. Over the 200 – 900 nm range, N_2*(0,0) at 337.1 nm is the dominant spectral feature. The spectral region between 388 nm and 400 nm is chosen to observe the change of the N_2^{+*}(0,0) emission at 391.4 nm and N_2^* emissions (bands (2,5) at 394.3 nm and (1,4) at 399.8 nm). Figure 6 (b.) shows spatially integrated spectra in four regions of interest.

The regions (1.) and (4.) are respectively the top and the bottom of the ring edges, where N_2^{+*} emission is clearly higher than that of N_2*. The N_2^{+*}(0,0) band emits strongest, but N_2^{+*}(1,1) emission at 388.4 nm is also weakly present. However, the region (2.) close to wire shows a dominant N_2*(1,4) band compared to N_2^{+*}. Also, the total intensity of plasma emission decreases significantly. For the region (3.) where corona emission is dominant, all the N_2* emissions are strong compared to N_2^{+*}. For the region (3.), the N_2^*(3,6) emission at 389.4 nm is also clearly visible (overlapped by the band structure of N_2^{+*}(0,0) in the regions 1. and 4.).

The plasma spectral emission in the ring region thus strongly differs from that close to the anode tip. As previously reported by Starikovskaia *et al* [33] , such a high level of N_2^{+*}(0,0) emission is evidence of a space charge region with a high local electric field. Consequently, the propagation of the plasma ring corresponds to the propagation of an ionization front.

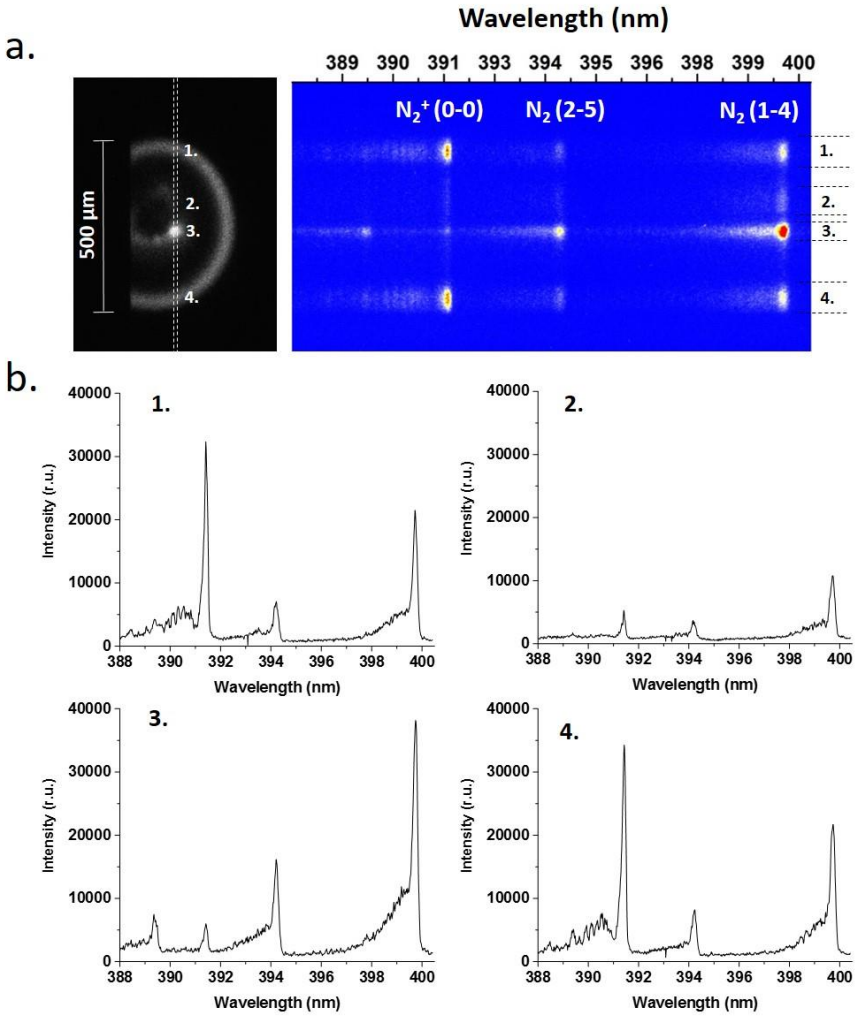

Figure 6 : ICCD image of the ring plasma at 19 ns with the slit position for OES sketched in dashed lines, and the corresponding emission spectrum at each position along the dimension of the slit (a). The spectra in the delimited regions (1.,2.,3.,4.) result from the binning of illuminated regions (b). The light is integrated 4 ns and accumulated over 5000 pulses (1000 pulses accumulated on the ICCD per acquisition, averaged 5 times).

The dynamics of plasma propagation is illustrated in Figure 7 with spatially-resolved spectra at several time delays, in the same experimental conditions as Figure 2 and Figure 6.

At 15 ns, the N_2^{+*} emission extends all along the plasma propagation path. This corresponds to the very beginning of the ring propagation phase depicted in Figure 2 at the same time delay. Because discharge ignition occurs at 10 ns and the integration time is 4 ns, this image integrates almost all the plasma propagation since its ignition. At 16 ns two intense heads of the ionization fronts are detached, while the light intensity decreases behind in the "channel". At 22 ns (close to the end of the ring propagation), the two fronts have propagated almost to their maximum distance. At this time, an appropriate colormap (not shown) reveals that weak emission of N_2^{+*} persists along the whole propagation path. Thus, the fronts are not fully disconnected from the anode tip.

The images at 32 ns and 37 ns show the propagation during the secondary plasma ignition phase depicted in Figure 2. Unlike the case of homogenous propagation and ring propagation phases, the "head" of the plasma is not defined by a dominant N_2^{+*} emission but rather by N_2*(1,4) emission, similar to region 3 in Figure 6(b.). In this case, all the N_2* bands emit more strongly in this spectral range than N_2^{+*}(0,0). This indicates that during the reverse breakdown (during the falling edge of the

voltage pulse in Figure 4 (a.)), the propagation of the secondary plasma is not driven by the same mechanism as the primary plasma but is likely related to the charges deposited after the primary propagation, as for the reverse breakdown mechanism reported in the literature [12], [22], [34]–[36].

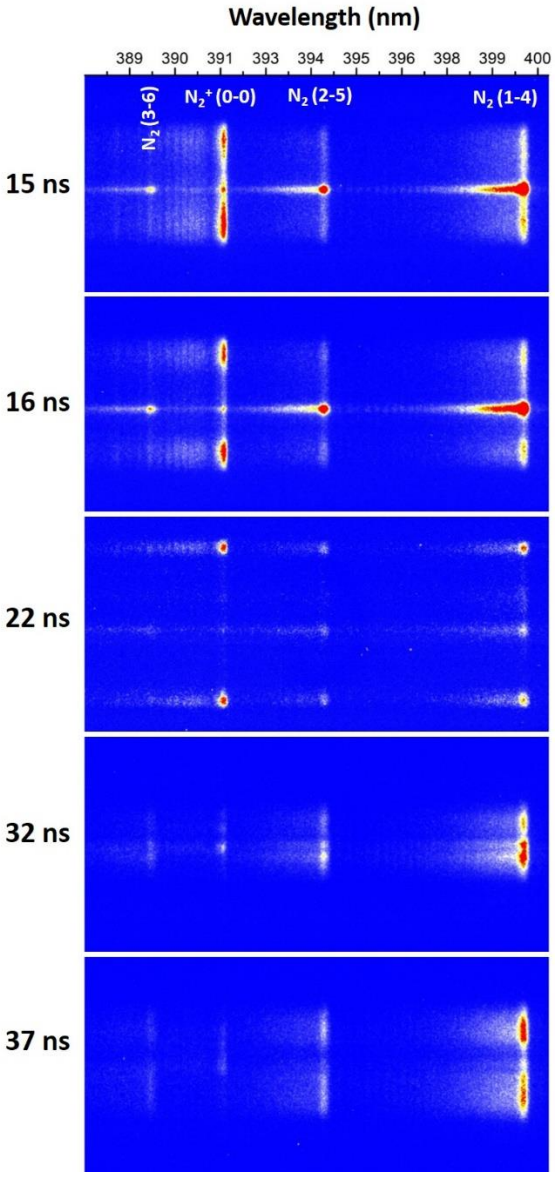

Figure 7: Spatially resolved spectra at selected times.The experimental conditions are the same as Figure 2 and Figure 6. The brightness scale is adjusted in order to highlight in red the emission at 391.4 nm (i.e. saturated in the corona discharge region at 15 ns and 16 ns).

To summarize, the propagation of the plasma on the Si-SiO_2 bilayer could be attributed to an ionization wave (IW). It is first characterized by dominant molecular excitation, as for streamers on SDBD [15]. The dominant excitation of N_2^{+}*(0,0) between 388 and 400 nm is evidence of a space charge region with a high electric field. The IW first propagates outward uniformly, leaving behind a filled bright circle indicating that the space charge is not yet sufficient to screen the electric field. Once screening occurs, the electric field behind the IW weakens. This region goes dark, thus creating the ring.

These are the steps expected for any positive streamer in the process of detaching from an anode. Consequently, the ring thickness reflects the balance between the excitation at the IW head and the recombination in the channel behind. The minimal size we measured in our condition was 28 µm (±3 µm), which is consistent with some of the smallest values reported in the literature [29]. The propagation velocity depicted in Figure 2 during the homogenous phase from (about 10^6 cm/s) is also in the range of previously reported values for positive surface IW [28], as for the lowest velocity during the ring propagation phase (about few 10^5 cm/s) [37]. Nevertheless, we point out that between 10 ns and 15 ns for the homogenous propagation phase and between 15 ns and 19 ns for the ring formation phase, the voltage amplitude increases (see Figure 4 (b.)) while the propagation velocity drops. This dependence of the propagation velocity on applied voltage is unusual because the propagation velocity typically increases with the applied voltage amplitude [19], [31].

3.3 Proposed mechanism of uniform propagation of the ionization wave

Uniform IW propagation is likely due to the use of the bilayer, as the material is the only variable in Figures 4 and 5. The plasma propagates on the dielectric SiO_2 layer, which covers the Si wafer. Silicon is well-known for its photo emissive properties. Photons with at least 1.1 eV of energy (i.e. wavelengths shorter than 800 nm) are absorbed and generate electron-hole pairs. The coupling interaction between an electron-ion plasma and electron-hole plasma has been extensively studied by the Eden group [38]–[41]. The high electric field of the plasma in the cathode fall region forces electrons to tunnel through the potential barrier at the interface between a semiconductor exposed directly to a low-pressure plasma. In the present paper, however, the plasma is isolated from the silicon by the 1 µm thick oxide layer, which is too thick to allow tunneling.

The propagating ionization front on the dielectric layer is both a source of photons, especially in the UV, and of high local electric field due to space charge. Based on the experimental SDBD configuration of Starikovskii *et al* [42], Babaeva *et al* [19] have modelled the propagation of the surface IW in positive and negative polarity. For positive polarity, a cathode sheath layer is formed near the surface. It leads to an elevation of the ionization front above the surface by about 20-40 µm and to a high electric field amplitude (several hundreds of kV/cm), which was also experimentally observed by Stepanyan *et al* [43].

The vertical electric field is perpendicular to the propagation surface. Consequently, once the electron-hole pairs have been generated in the Si bulk, the electrons are pulled upward to the Si-SiO_2 interface and the holes are pushed downward into the silicon bulk. The charge separation between electrons and holes leads to the formation of space charge inside the silicon. The time scale of electron-hole generation and the resulting Coulomb interaction is about 10^{-5} ns according to Huber *et al* [44]. Therefore, it can be considered as instantaneous at the time scale of plasma propagation. The electron mobility in silicon is about 1400 $cm^2V^{-1}s^{-1}$ and about 400 $cm^2V^{-1}s^{-1}$ for the holes. Assuming an electric field of about 10 kV/cm in the silicon close to the interface, the holes can drift at 4µm/ns and the electrons at 14 µm/ns. The electrons would then accumulate very quickly at the Si-SiO_2 interface because the oxide layer is too thick (1 µm) to allow electron tunneling. Because the ionization front is both a source of photons and intense local electric field, plasma propagation would occur simultaneously with the accumulation of negative charge at the interface in the immediate vicinity of the front, as sketched in Figure 8. This interfacial space charge would be localized and synchronized with ionization front propagation, and may "guide" the IW toward the surface. Nijdam *et al* [25] demonstrated the guiding of positive streamers in air by free electrons generated by laser illumination,

but in our case the guiding electrons would be the accumulated photoelectrons at the Si-SiO_2 interface that do not contribute directly to avalanche ionization.

With a statistical photon transport and photoionization model embedded into a fluid-based plasma transport model, Xiong and Kushner [32] have studied the origin of path deviation and branching of a positive streamer in air at atmospheric pressure. The initially uniform space charge layer (SCL) is quickly perturbed (2 ns after the discharge ignition) by back-travelling secondary avalanches initiated by random photoelectrons ahead of the front. The induced asymmetry in the SCL could lead to path deviation or branching, depending on the strength of the secondary avalanche. The authors have emphasized the importance of the local environment of the streamer head and on the magnitude of the electric field ahead of the streamer. They have also shown that if the majority of the avalanches occurs in closer proximity to the front, the probability of path deviation and branching decreases. Thus, when the IW propagates on the Si-SiO_2 bilayer, the interfacial space charge concentrates the electric field near the front, and likewise the secondary avalanches, as sketched in Figure 8. This could inhibit branching and preserve the initial shape of the SCL during propagation. It could also result in the drop of the propagation velocity while the voltage amplitude is still increasing, as depicted in Figure 2.

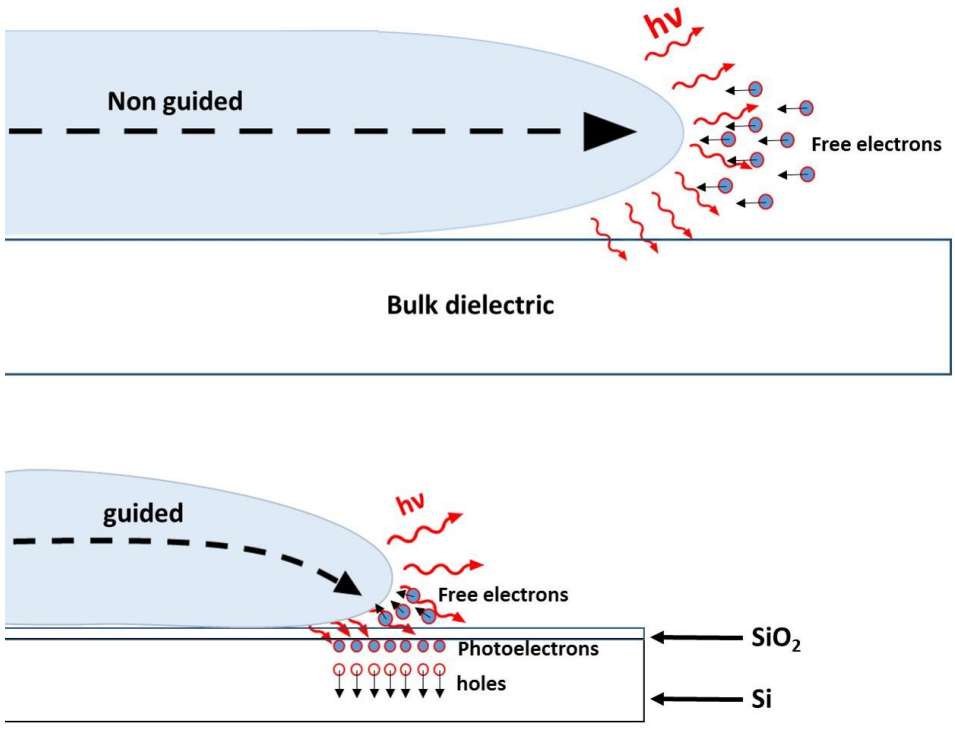

Figure 8 : Schematic illustration of IW propagation on the Si-SiO_2 bilayer, with the local accumulation of negative space charge at the interface, due to photoelectric conversion in the Si bulk. The IW is then "guided" toward the surface, with a tilt in its propagation direction compared to the propagation on a bulk dielectric.

To verify the presence of a photoelectric effect, Figure 9 shows the effect of focusing a continuous wave laser at 532 nm on the surface, ahead of the IW, for the discharge conditions of Figure 2 (the applied voltage is 2 kV). The laser photon energy is 2.3 eV, which is sufficient to generate electron-hole pairs in silicon. To focus the laser and perform imaging, we employed the Raman micro-spectrometer described in Pai *et al* [26] using a 3X visible objective. As such, only visible emission was acquired in the images of Figure 9, with the laser spot filtered out by a notch filter. The laser spot was

approximately 40 µm in diameter and the power of the laser beam at the surface is 0.7 mW, yield a power density of about 60 $W.cm^{-2}$.

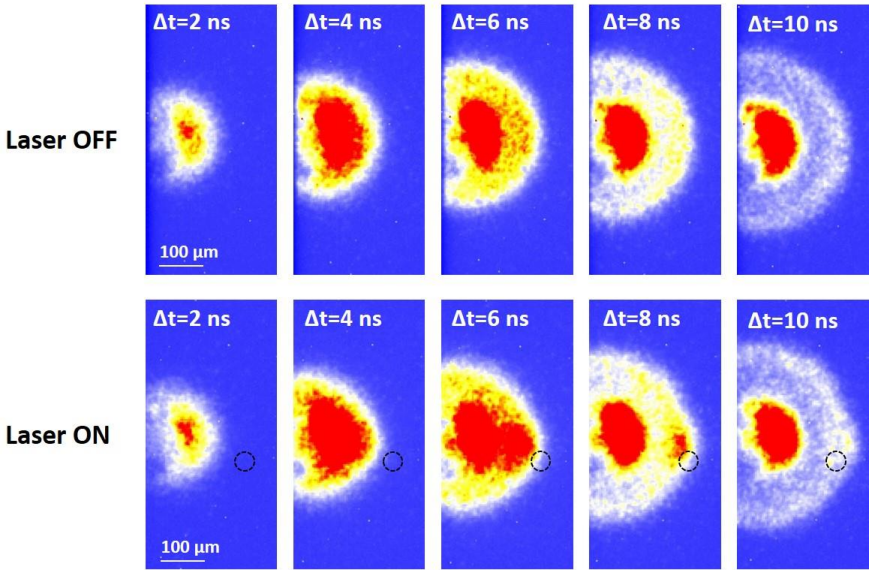

Figure 9 : Images in the visible range of plasma propagation at several times after the plasma ignition for an applied voltage of 2 kV, with the laser off (top) and on (bottom). The laser spot position (~ 40 µm diameter) is sketched in dashed lines. The brightness scale (same for all images) is adjusted in order to highlight the small change of light emission at the plasma edges at ⊿t = 8 ns and 10 ns and is saturated close to the anode tip. The images are integrated 4 ns and accumulated over 1000 pulses.

At Δt=2 ns after plasma ignition, the plasma propagation is not affected by the laser illumination. However at Δt= 4 ns, with the laser on, the plasma bulges slightly in the direction of the laser spot. At this time, the IW has not yet reached the spot. At Δt=6 ns, the bulge of the IW becomes prominent. At Δt= 8 ns, a very localized region of high intensity close to the laser spot is clearly visible. Without this external illumination at the same time delay, the ring-shaped ionization front remains quite homogenous. At Δt=10 ns the total light intensity decreases, but the deformation of the front is still visible. Thus, the external illumination clearly influences plasma propagation, even before the plasma reaches the laser spot. This may be possible if the laser-generated electron-hole plasma causes a local enhancement of the electric field, due to the negative SCL just under the SiO_2 layer. This local field may act at a distance to deform the IW front.

Figure 10 compares additional ICCD images in the same experimental conditions than for the Figure 9, for the fixed time delay of Δt= 10 ns. Right after the laser is turned on, an image resulting of 1000 pulses accumulation on the CCD is taken. Due to the limitation of the frame per second number allowing by the ICCD camera in the region of interest, it takes approximately one minute. Then, keeping the plasma on, the laser is turned off and another image is taken immediately afterwards. Finally, still keeping the plasma on with the laser off, images are taken every subsequent 5 minutes.

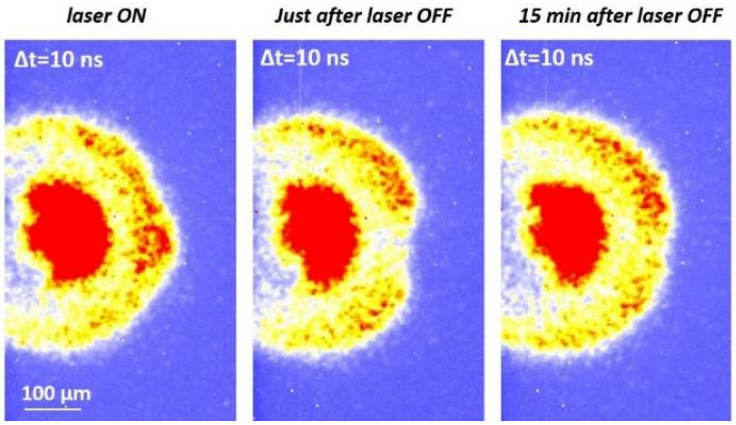

Figure 10 : ICCD images of the plasma 10 ns after plasma ignition during and after laser illumination. The brightness scale (same for all images) is adjusted in order to highlight the change of light emission at the plasma edges at 10 ns and is saturated close to the anode tip. The images are integrated 4 ns and accumulated over 1000 pulses.

Just after the laser is turned off, the plasma does not recover its initial state (Figure 10, middle). Instead, a "void" of plasma is clearly visible at the location of previously enhanced light emission (Figure 10, left). However, 15 minutes later (Figure 10, right), the plasma has almost recovered its initial propagation state (Figure 9, top). This observation clearly suggests that a memory effect affects plasma propagation, on a time scale of minutes after the cessation of the laser irradiation. This "void" of plasma was only observed following simultaneous laser illumination and plasma generation. When the illuminated region was pre-exposed with laser without the plasma, followed by plasma ignition with the laser turned off, the "void" was not observed. In studies of the Si-SiO_2 interface when used for second harmonic generation, several authors have reported a memory effect after the cessation of laser illumination lasting several hundred seconds or more. They attributed the memory effect to the relaxation of the Si-SiO_2 interface related to the trapping mechanism of electrons [45]–[47] and holes [48]. Furthermore, the influence of the laser illumination on plasma propagation implies that the laser spot is clearly intrusive. Care must be taken to account for the influence of the light source on the plasma, not only when *in situ* optical diagnostics are performed, but also several minutes after the cessation of laser illumination due to the memory effect.

A memory effect is apparent with the addition of the continuous wave laser but not with the plasma alone, under the conditions of the present study. We varied the pulse repetition rate from 10 to 500 Hz, but no changes to the plasma were observed. Therefore, there is no discernable memory effect due to the pulse repetition rate at 50 Hz. Furthermore, the ring IW is even observed upon applying the first pulse over a region of the surface previously unexposed to plasma, which implies that the accumulated effect of previous pulses is not required to stabilize IW propagation.

The role of the Si-SiO_2 interface in IW propagation may be examined by testing different bilayers, such as Si-Al_2O_3 (Figure 11). An amorphous alumina film (453 nm thick) was deposited at room temperature on the polished side of a bare silicon wafer (p-type) using a dual ion beam sputtering Nordiko™ chamber, as described in Camelio *et al* [49] and Babonneau *et al* [50]. In contrast to the Si-SiO_2 bilayer, the plasma is not stable with the Si-Al_2O_3 bilayer. At an applied voltage of 2 kV, the plasma was only ignited 14 out of 100 pulses and remained localized close to the wire. In order to ignite a plasma with almost each pulse, the applied voltage had to be increased to 4.5 kV, producing very disturbed ring IW shapes. Unlike for the Si-SiO_2 bilayer, it was not possible in this case to follow the plasma propagation as a function time delay due to discharge instability.

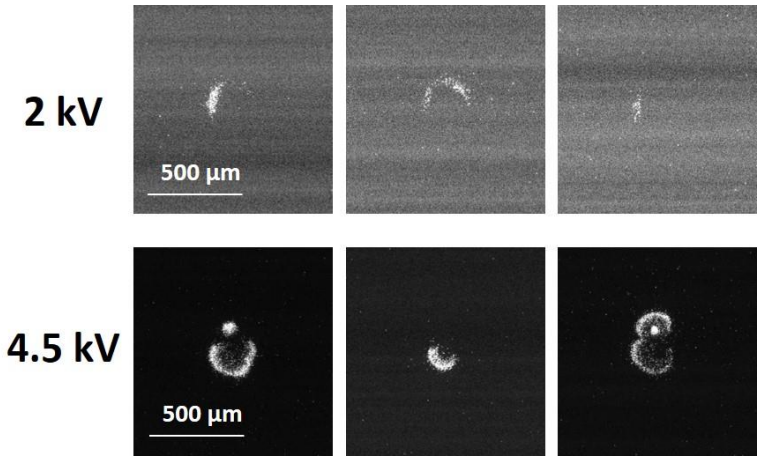

Figure 11 : Single shot ICCD images of plasma generated on the Si-Al_2O_3 bilayer, at applied voltages of 2 kV and 4.5 kV. The same time delay (23 ns) and integration time (4 ns) are used for all images.

However, if a 345 nm thick alumina layer is deposited on the Si-SiO_2 bilayer, creating a Si-SiO_2-Al_2O_3 trilayer, the ring IW is preserved, as shown in Figure 12 (b.). Consequently, even if the material facing the plasma is changed, the plasma properties are preserved when the Si-SiO_2 interface is present underneath. This observation clearly highlights the influence of the interface on the ring IW mechanism. Figure 12 (c.) shows the plasma expansion when the third layer is a 300 nm of UltraNanoCrystallineDiamond (UNCD®, provided by Advanced Diamond Technology), made of small nanocrystalline diamond grains from 3 nm to 5 nm. For the same discharge conditions as for Figure 12 (a.) and Figure 12 (b.), the propagation distance is increased by 30 %. Using spectroscopic ellipsometry at 1600 nm, we measured the indices of refraction of Si, SiO_2, Al_2O_3, and UNCD to be respectively 3.5, 1.4, 1.6 and 2.3. Between the (a.) and (b.) cases, the propagation distance is not affected while the permittivity (ε) value increases. Between the (b.) and (c.) cases, the plasma propagation increases with ε. This trend contrasts with the observations of Sokolova *et al* [51], where the plasma length decreases with increasing ε value. Thus, the propagation distance in our case cannot be attributed simply to a change in permittivity. These plasma-trilayer interactions will be investigated in future work. Thus, this multi-layer approach could be of interest for further studies on plasma-surface interactions with the generation of a very stable discharge in ambient air, propagating over a wide range of possible third layer materials.

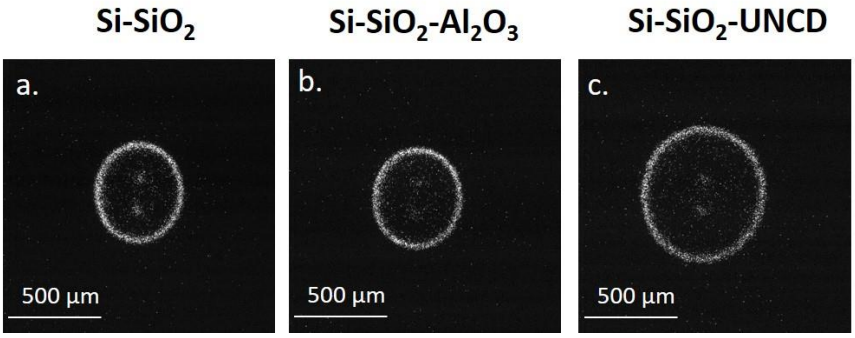

Figure 12 : Single shot ICCD image of plasma generated on the Si-SiO_2 bilayer (left) (a.), Si-SiO_2-Al_2O_3 trilayer (b.) and Si-SiO_2-UNCD trilayer (c.) in the same operating conditions, at an applied voltages of 2 kV. The time delay is fixed at 21 ns and the exposure time is 4 ns.

These results using different bilayers point to the required presence of the Si-SiO_2 interface. The formation of defects at the Si-SiO_2 interface introduces additional energy levels into the forbidden band [52]. Defects are of great importance in MOS capacitors and have been extensively characterized

[53]–[57]. Defects are electrically active, with the sign depending on the charge captured, and the capture cross section depends on the applied electric field and temperature [58]. The plasma-SiO_2-Si structure resembles a MOS capacitor device, where the plasma plays the role of the metal electrode. Changing the electrical nature of the silicon and the oxide-semiconductor interface from Si-SiO_2 to Si-Al_2O_3 may alter the electrical response of the system. The electric properties of the silicon used, when exposed to the high value of the IW local electric field, may also play a role [59]. However, a detailed study of the interface in terms of band structure is beyond the scope of this paper.

Also, we can draw an analogy between the branching inhibition with the ring IW mechanism proposed in Figure 8 and the inception clouds and diffuse volume discharges observed in bulk gases at low pressure [60], [61]. The latter also initially exhibit a circular (spherical) front with a homogenous phase (cloud), followed by a slower expanding shell-like phase. Then the shell-like phase can break up into faster streamers. The difference in surface plasma propagation between glass versus the Si-SiO_2 bilayer is akin to the difference in behavior between the volume plasma expansion in pure gases versus air. While the shell-like phase is common in air, the destabilization into streamers occurs immediately in pure gases such as nitrogen. Photo-ionization is particularly prevalent in air and is suspected to provide a large density of seed electrons, smoothing the cloud propagation. This is analogous to our hypothesis on the role of photoelectrons in the ring IW development on the Si-SiO_2 bilayer.

IV Conclusion

In this paper, we have studied the modification of the plasma propagation dynamics of a nanosecond pulsed SDBD in positive polarity when a Si-SiO_2 bilayer (Silicon wafer covered by a 1 µm thick layer of SiO_2) is used as a propagation surface instead of a classical bulk dielectric. Unlike the latter case, the plasma propagates uniformly without any branching, leading to the formation of a well-defined ring structure. The ring corresponds to a homogenous ionization front (~40 µm thick), exhibiting a high N_2^+* emission. From pulse to pulse, the discharge demonstrates high stability and reproducibility. To the best of our knowledge, this is the first report of such a uniform propagation for a surface discharge in ambient air at atmospheric pressure, especially for positive polarity discharges where plasma propagation is cathode-directed. The reproducibility and control of the plasma in pulse-to-pulse operation are also difficult to obtain otherwise, especially in ambient air. The photons emitted by the ionization wave may generate charges at the Si-SiO_2 interface by the photoelectric effect. As the generation of an electron-hole pair at the interface is extremely fast, the surface electric field may change instantaneously and very locally at the front of the IW. This synergetic effect between the photons emitted by the plasma and the surface electrical response, with accumulated photoelectrons at the Si-SiO_2 interface, may “guide” the IW toward the surface and inhibit branching of the ionization wave. The influence of 532 nm laser illumination on the plasma propagation and the sensitivity of the plasma to the interface (Si-SiO_2 vs Si-Al_2O_3) provides evidence for this plasma-multi-layer coupling mechanism.

The ring-shaped ionization wave in ambient air also offers opportunities to explore plasma surface interaction with a stable and localized discharge. Because this features are still preserved with the deposition of a third thin dielectric layer on the Si-SiO_2 bilayer (trilayer structure), it is therefore possible to potentially change the nature of the third layer over a wide range of materials. This multi-layer approach could then be used for local surface modifications with a stable surface plasma generated in ambient air. The high degree of reproducibility and stability of this discharge may also offer perspectives for flow control applications. Additional layers could potentially be used to increase

the plasma size and avoid breakdown damage of the surface if higher voltage pulse amplitudes must be applied. The electrode geometry could be engineered to guide the plasma propagation in a preferential direction, in order to generate a net electrohydrodynamic force. Also, the sensitivity of the plasma to external illumination could potentially be exploited to influence the propagation direction.

Acknowledgements

This work was supported by the Agence Nationale de la Recherche programs JCJC PLASMAFACE (ANR-15-CE06-0007-01) and the "Investissements d'Avenir" program LABEX INTERACTIFS (ANR-11-LABX-0017-01) of the French government, and the CPER-FEDER program of the Région Nouvelle Aquitaine. The authors are grateful to Frédéric Pailloux for the valuable contributions and discussions concerning the present study.

References

[1] N. Benard and E. Moreau, "Role of the electric waveform supplying a dielectric barrier discharge plasma actuator," *Appl. Phys. Lett.*, vol. 100, no. 19, p. 193503, 2012.

[2] K. D. Bayoda, N. Benard, and E. Moreau, "Nanosecond pulsed sliding dielectric barrier discharge plasma actuator for airflow control: Electrical, optical, and mechanical characteristics," *J. Appl. Phys.*, vol. 118, no. 6, p. 063301, 2015.

[3] S. B. Leonov, I. V Adamovich, and V. R. Soloviev, "Dynamics of near-surface electric discharges and mechanisms of their interaction with the airflow," *Plasma Sources Sci. Technol.*, vol. 25, no. 6, p. 063001, 2016.

[4] S. M. Starikovskaia, "Plasma-assisted ignition and combustion: nanosecond discharges and development of kinetic mechanisms," *J. Phys. D. Appl. Phys.*, vol. 47, no. 35, p. 353001, 2014.

[5] M. Hähnel, V. Brüser, and H. Kersten, "Diagnostics of SiOx-containing layers deposited on powder particles by dielectric barrier discharge," *Plasma Process. Polym.*, vol. 4, no. 6, pp. 429–637, 2007.

[6] J. Voráč, P. Synek, P. Dvořák, and T. Hoder, "Time- and space-resolved LIF measurement of the concentration of OH radicals generated by surface barrier discharge emerging from liquid water," *Plasma Sources Sci. Technol.*, vol. 28, no. 10, p. 105008, 2019.

[7] R. Brandenburg, "Dielectric barrier discharges: Progress on plasma sources and on the understanding of regimes and single filaments," *Plasma Sources Sci. Technol.*, vol. 26, no. 5, p. 053001, 2017.

[8] J. Reece Roth and X. Dai, "Optimization of the aerodynamic plasma actuator as an electrohydrodynamic (EHD) electrical device," *Collect. Tech. Pap. - 44th AIAA Aerosp. Sci. Meet.*, vol. 19, pp. 14604–14631, 2006.

[9] N. E. Fine and S. J. Brickner, "Plasma catalysis for enhanced-thrust single dielectric barrier discharge plasma actuators," *AIAA J.*, vol. 48, no. 12, pp. 2979–2982, 2010.

[10] D. F. Opaits, S. S. Zaidi, M. N. Shneider, R. B. Miles, A. V. Likhanskii, and S. O. Macheret, "Suppression of dielectric barrier discharge charge buildup using a partially conducting thin film," *39th AIAA Fluid Dyn. Conf.*, vol. AIAA Paper, no. 4189, 2009.

[11] A. Starikovskiy and R. B. Miles, "Dielectric Barrier Discharge Control and Thrust Enhancement

by Diode Surface," *51st AIAA Aerosp. Sci. Meet. Incl. New Horizons Forum Aerosp. Expo.*, 2013.

[12] A. Starikovskiy and R. B. Miles, "Dielectric Barrier Discharge Control and Thrust Enhancement by Diode Surface," *52nd Aerosp. Sci. Meet.*, 2014.

[13] S. B. Leonov, V. Petrishchev, and I. V Adamovich, "Dynamics of energy coupling and thermalization in barrier discharges over dielectric and weakly conducting surfaces on μ s to ms time scales," *J. Phys. D. Appl. Phys.*, vol. 47, no. 46, p. 465201, 2014.

[14] S. A Stepanyan, A Y. Starikovskiy, N. A Popov, and S. M. Starikovskaia, "A nanosecond surface dielectric barrier discharge in air at high pressures and different polarities of applied pulses: transition to filamentary mode," *Plasma Sources Sci. Technol.*, vol. 23, no. 4, p. 045003, 2014.

[15] C. Ding, A. Y. Khomenko, S. A. Shcherbanev, and S. M. Starikovskaia, "Filamentary nanosecond surface dielectric barrier discharge. Experimental comparison of the streamer-to-filament transition for positive and negative polarities," *Plasma Sources Sci. Technol.*, vol. 28, no. 8, p. 085005, 2019.

[16] D. Z. Pai, S. Stauss, and K. Terashima, "Surface dielectric barrier discharges exhibiting field emission at high pressures," *Plasma Sources Sci. Technol.*, vol. 23, no. 2, p. 025019, 2014.

[17] D. Z. Pai, S. Stauss, and K. Terashima, "Field-emitting Townsend regime of surface dielectric barrier discharges emerging at high pressure up to supercritical conditions," *Plasma Sources Sci. Technol.*, vol. 24, no. 2, p. 25021, 2015.

[18] M. Kanno, R. Tanaka, S. Stauss, T. Ito, and K. Terashima, "Generation of field-emitting surface dielectric barrier discharges in Ar and N2," *AIP Adv.*, vol. 9, no. 5, p. 0555111, 2019.

[19] N. Y. Babaeva, D. V. Tereshonok, and G. V. Naidis, "Fluid and hybrid modeling of nanosecond surface discharges: Effect of polarity and secondary electrons emission," *Plasma Sources Sci. Technol.*, vol. 25, no. 4, p. 44008, 2016.

[20] V. R. Soloviev and V. M. Krivtsov, "Numerical modelling of nanosecond surface dielectric barrier discharge evolution in atmospheric air," *Plasma Sources Sci. Technol.*, vol. 27, no. 11, p. 102548, 2018.

[21] B. M. Goldberg, P. S. Böhm, U. Czarnetzki, I. V Adamovich, and W. R. Lempert, "Electric field vector measurements in a surface ionization wave discharge," *Plasma Sources Sci. Technol.*, vol. 24, no. 5, p. 055017, 2015.

[22] M. Simeni Simeni, Y. Tang, K. Frederickson, and I. V Adamovich, "Electric field distribution in a surface plasma flow actuator powered by ns discharge pulse trains," *Plasma Sources Sci. Technol.*, vol. 27, no. 10, p. 104001, 2018.

[23] V. Petrishchev, S. Leonov, and I. V. Adamovich, "Studies of nanosecond pulse surface ionization wave discharges over solid and liquid dielectric surfaces," *Plasma Sources Sci. Technol.*, vol. 23, no. 6, p. 065022, 2014.

[24] E. Takahashi, S. Kato, A. Sasaki, Y. Kishimoto, and H. Furutani, "Controlling branching in streamer discharge by laser background ionization," *J. Phys. D. Appl. Phys.*, vol. 44, no. 7, p. 075204, 2011.

[25] S. Nijdam, J. Teunissen, E. Takahashi, and U. Ebert, "The role of free electrons in the guiding of positive streamers," *Plasma Sources Sci. Technol.*, vol. 25, no. 4, p. 44001, 2016.

[26] D. Z. Pai, F. Pailloux, and D. Babonneau, " In situ Raman spectroscopy of nanostructuration by surface plasmas generated on alumina thin film-silicon bilayers ," *Plasma Sources Sci. Technol.*, vol. 28, no. 8, p. 085007, 2019.

[27] K. V Kozlov, H. Wagner, R. Brandenburg, and P. Michel, “Spatio-temporally resolved spectroscopic diagnostics of the barrier discharge in air at atmospheric pressure,” *J. Phys. D. Appl. Phys.*, vol. 34, no. 21, pp. 3164–3176, 2001.

[28] H. Grosch, T. Hoder, K. D. Weltmann, and R. Brandenburg, “Spatio-temporal development of microdischarges in a surface barrier discharge arrangement in air at atmospheric pressure,” *Eur. Phys. J. D*, vol. 60, no. 3, pp. 547–553, 2010.

[29] H. Höft, M. M. Becker, and M. Kettlitz, “Correlation of axial and radial breakdown dynamics in dielectric barrier discharges,” *Plasma Sources Sci. Technol.*, vol. 27, no. 3, 2018.

[30] S. Rosin, “Inverse Cassegrainian Systems,” *Appl. Opt*, vol. 7, pp. 1483–1497, 1968.

[31] T. Hoder, P. Synek, and J. Voráč, “Charge transfer equilibrium in surface barrier discharge: continuous current and negative ion-driven ionisation wave,” *Plasma Sources Sci. Technol.*, vol. 28, no. 10, p. 105016, 2019.

[32] Z. Xiong and M. J. Kushner, “Branching and path-deviation of positive streamers resulting from statistical photon transport,” *Plasma Sources Sci. Technol.*, vol. 23, no. 6, p. 065041, 2014.

[33] S. M. Starikovskaia, K. Allegraud, O. Guaitella, and A. Rousseau, “On electric field measurements in surface dielectric barrier discharge,” *J. Phys. D. Appl. Phys.*, vol. 43, no. 12, p. 124007, 2010.

[34] A. V. Likhanskii, M. N. Shneider, S. O. Macheret, and R. B. Miles, “Modeling of dielectric barrier discharge plasma actuators driven by repetitive nanosecond pulses,” *Phys. Plasmas*, vol. 14, no. 7, p. 073501, 2007.

[35] A. Y. Starikovskii, A. A. Nikipelov, M. M. Nudnova, and D. V. Roupassov, “SDBD plasma actuator with nanosecond pulse-periodic discharge,” *Plasma Sources Sci. Technol.*, vol. 18, no. 3, p. 034015, 2009.

[36] N. Benard, N. Zouzou, A. Claverie, J. Sotton, and E. Moreau, “Optical visualization and electrical characterization of fast-rising pulsed dielectric barrier discharge for airflow control applications,” *J. Appl. Phys.*, vol. 111, no. 3, p. 033303, 2012.

[37] J. P. Boeuf and L. C. Pitchford, “Electrohydrodynamic force and aerodynamic flow acceleration in surface dielectric barrier discharge,” *J. Appl. Phys.*, vol. 97, no. 10, p. 103307, 2005.

[38] N. P. Ostrom and J. G. Eden, “Microcavity plasma photodetectors: Photosensitivity, dynamic range, and the plasma-semiconductor interface,” *Appl. Phys. Lett.*, vol. 87, no. 14, pp. 1–3, 2005.

[39] C. J. Wagner, P. A. Tchertchian, and J. G. Eden, “Coupling electron-hole and electron-ion plasmas: Realization of an npn plasma bipolar junction phototransistor,” *Appl. Phys. Lett.*, vol. 97, no. 13, pp. 1–4, 2010.

[40] P. A. Tchertchian, C. J. Wagner, J. J. Houlahan, B. Li, D. J. Sievers, and J. G. Eden, “Control of the interface between electron-hole and electron-ion plasmas: Hybrid semiconductor-gas phase devices as a gateway for plasma science,” *Contrib. to Plasma Phys.*, vol. 51, no. 10, pp. 889–905, 2011.

[41] B. Li, T. J. Houlahan, C. J. Wagner, and J. G. Eden, “Modulating the secondary electron emission coefficient at the base-collector interface of the plasma bipolar junction transistor,” *Appl. Phys. Lett.*, vol. 102, no. 8, 2013.

[42] A. Y. Starikovskii, A. A. Nikipelov, M. M. Nudnova, and D. V. Roupassov, “SDBD plasma

actuator with nanosecond pulse-periodic discharge," *Plasma Sources Sci. Technol.*, vol. 18, no. 3, p. 034015, 2009.

[43] S. A. Stepanyan, V. R. Soloviev, and S. M. Starikovskaia, "An electric field in nanosecond surface dielectric barrier discharge at different polarities of the high voltage pulse: Spectroscopy measurements and numerical modeling," *J. Phys. D. Appl. Phys.*, vol. 47, no. 48, p. 485201, 2014.

[44] R. Huber, F. Tauser, A. Brodschelm, M. Bichler, G. Abstreiter, and A. Leitenstorfer, "How many-particle interactions develop after ultrafast excitation of an electron-hole plasma," *Nature*, vol. 414, no. 6861, pp. 286–289, 2001.

[45] J. G. Mihaychuk, J. Bloch, Y. Liu, and H. M. van Driel, "Time-dependent second-harmonic generation from the Si–SiO_2 interface induced by charge transfer," *Opt. Lett.*, vol. 20, no. 20, p. 2063, 1995.

[46] J. Bloch, J. G. Mihaychuk, and H. M. van Driel, "Electron Photoinjection from Silicon to Ultrathin SiO2 Films via Ambient Oxygen," *Phys. Rev. Lett.*, vol. 77, no. 5, pp. 920–923, 1996.

[47] N. Shamir, J. G. Mihaychuk, and H. M. van Driel, "Transient charging and slow trapping in ultrathin SiO2 films on Si during electron bombardment," *J. Vac. Sci. Technol. A Vacuum, Surfaces, Film.*, vol. 15, no. 4, pp. 2081–2084, 1997.

[48] W. Wang *et al.*, "Coupled electron-hole dynamics at the Si/SiO2 interface," *Phys. Rev. Lett.*, vol. 81, no. 19, pp. 4224–4227, 1998.

[49] S. Camelio, D. Babonneau, D. Lantiat, L. Simonot, and F. Pailloux, "Anisotropic optical properties of silver nanoparticle arrays on rippled dielectric surfaces produced by low-energy ion erosion," *Phys. Rev. B - Condens. Matter Mater. Phys.*, vol. 80, no. 15, pp. 1–10, 2009.

[50] D. Babonneau, E. Vandenhecke, and S. Camelio, "Formation of nanoripples on amorphous alumina thin films during low-energy ion-beam sputtering: Experiments and simulations," *Phys. Rev. B - Condens. Matter Mater. Phys.*, vol. 95, no. 8, pp. 1–16, 2017.

[51] M. V. Sokolova, V. V. Voevodin, J. I. Malakhov, N. L. Aleksandrov, E. M. Anokhin, and V. R. Soloviev, "Barrier properties influence on the surface dielectric barrier discharge driven by single voltage pulses of different duration," *J. Phys. D. Appl. Phys.*, vol. 52, no. 32, p. 324001, 2019.

[52] T. Sakurai and T. Sugano, "Theory of continuously distributed trap states at Si-SiO2 interfaces," *J. Appl. Phys.*, vol. 52, no. 4, pp. 2889–2896, 1981.

[53] F. P. Heiman and G. Warfield, "The Effects of Oxide Traps on the MOS Capacitance," *IEEE Trans. Electron Devices*, vol. 12, no. 4, pp. 167–178, 1965.

[54] T. Katsube, K. Kakimoto, and T. Ikoma, "Temperature and energy dependences of capture cross sections at surface states in Si metal-oxide-semiconductor diodes measured by deep level transient spectroscopy," *J. Appl. Phys.*, vol. 52, no. 5, pp. 3504–3508, 1981.

[55] W. D. Eades and R. M. Swanson, "Improvements in the determination of interface state density using deep level transient spectroscopy," *J. Appl. Phys.*, vol. 56, no. 6, pp. 1744–1751, 1984.

[56] D. Vuillaume and J. C. Bourgoin, "Characterization of Si-SiO2 interface states: Comparison between transient capacitance and conductance techniques," *J. Appl. Phys.*, vol. 58, no. 5, pp. 2077–2079, 1985.

[57] D. M. Fleetwood *et al.*, "Effects of oxide traps, interface traps, and '"border traps"' on metal-

oxide-semiconductor devices," *J. Appl. Phys.*, vol. 73, no. 10, pp. 5058–5074, 1993.

[58] D. J. DiMaria, *the Properties of Electron and Hole Traps in Thermal Silicon Dioxide Layers Grown on Silicon*, S.T. Pante. Pergamon Press Inc., 1979.

[59] M. Morohashi, N. Sawaki, and I. Akasaki, "Electron mobility and drag effect in p-type silicon," *Jpn. J. Appl. Phys.*, vol. 24, no. 6 R, pp. 732–736, 1985.

[60] S. Chen, L. C. J. Heijmans, R. Zeng, S. Nijdam, and U. Ebert, "Nanosecond repetitively pulsed discharges in N2-O2 mixtures: Inception cloud and streamer emergence," *J. Phys. D. Appl. Phys.*, vol. 48, no. 17, 12pp, 2015.

[61] T. Hoder, Z. Bonaventura, V. Prukner, F. J. Gordillo-Vazquez, and M. Šimek, "Emerging and expanding streamer head in low-pressure air," *Plasma Sources Sci. Technol.*, vol. 29, no. 03LT01, 7pp, 2020.